ADVANCED FUNCTIONAL MATERIALS
www.afm-journal.de

Bespoke Metal Nanoparticle Synthesis at Room Temperature and Discovery of Chemical Knowledge on Nanoparticle Growth via Autonomous Experimentations

Hyuk Jun Yoo, Nayeon Kim, Heeseung Lee, Daeho Kim, Leslie Tiong Ching Ow, Hyobin Nam, Chansoo Kim, Seung Yong Lee, Kwan-Young Lee, Donghun Kim,* and Sang Soo Han**

The optimization of nanomaterial synthesis using numerous synthetic variables is considered to be an extremely laborious task because conventional combinatorial explorations are prohibitively expensive. In this work, an autonomous experimentation platform developed for the bespoke design of metal nanoparticles (NPs) with targeted optical properties is reported. This platform operates in a closed-loop manner between the batch synthesis module of metal NPs and the UV–vis spectroscopy module, based on the feedback of the AI optimization modeling. With silver (Ag) NPs as a representative example, it is demonstrated that the Bayesian optimizer implemented with the early stopping criterion can efficiently produce Ag NPs at room temperature precisely possessing the desired absorption spectra within only 200 iterations (when optimizing among five aqueous synthetic reagents). In addition to the outstanding material developmental efficiency, the analysis of synthetic variables further reveals a novel chemistry involving the quantitative effects of citrate in Ag NP synthesis. The amount of citrate is key to controlling the competition between spherical and plate-shaped NPs and, as a result, affects the shapes of the absorption spectra as well. This study highlights both capabilities of the platform to enhance search efficiencies and to provide novel chemical knowledge by analyzing datasets accumulated from autonomous experimentations.

1. Introduction

Nanoparticles (NPs) have extensively been utilized in various applications including solar cells,[1–4] catalysis,[5–7] and chemical sensors[8–10] due to the wide tunability of electronic and optical properties through the manipulation of their size, shape, and surface states.[11–14] In particular, the wet chemical synthesis of colloidal NPs has attracted much attention mainly because of its low-cost and solution-based processing. The properties of colloidal NPs are known to be highly affected by numerous synthetic variables, including solution volume,[15,16] concentration,[17–19] injection rate,[20,21] synthetic sequences,[22] and aging time.[23,24] Currently, combinatorial experiments (*aka* Edisonian approach) are often used to design NPs that exhibit desired properties, but these trial-and-error-based methods are extremely laborious and time-consuming, which inspires the need for an approach of more intelligent explorations over large chemical spaces.

H. J. Yoo, N. Kim, H. Lee, D. Kim, L. T. C. Ow, C. Kim, D. Kim, S. S. Han
Computational Science Research Center
Korea Institute of Science and Technology
Seoul 02792, Republic of Korea
E-mail: donghun@kist.re.kr; sangsoo@kist.re.kr

The ORCID identification number(s) for the author(s) of this article can be found under https://doi.org/10.1002/adfm.202312561

DOI: 10.1002/adfm.202312561

H. J. Yoo, D. Kim, K.-Y. Lee
Department of Chemical and Biological Engineering
Korea University
Seoul 02841, Republic of Korea
E-mail: kylee@korea.ac.kr

N. Kim
Department of Chemistry
Korea University
Seoul 02841, Republic of Korea

H. Lee
Department of Materials Science and Engineering
Korea University
Seoul 02841, Republic of Korea

H. Nam, S. Y. Lee
Materials Architecturing Research Center
Korea Institute of Science and Technology
Seoul 02792, Republic of Korea

Autonomous material developments based on artificial intelligence (AI) have recently emerged as a promising direction to maximize the search efficiency over various classes of materials, including organic molecules,[25–27] perovskite,[28,29] colloidal quantum dots,[30] and nanoparticles.[31–35] For example, Abolhasani and coworkers[30] adopted AI in their quantum dot developmental systems, where only 920 trial experiments were sufficient to reach the target properties. Similarly, Cooper and coworkers[36] reported an autonomous developmental system for finding photocatalytic materials where ten environmental synthetic conditions were successfully optimized with less than 700 experiments in a week, which is a surprisingly small number given the vast parameter spaces over ten dimensions. Such dramatic enhancements in the search efficiency were achieved mainly because AI models effectively learn the correlations between synthetic conditions and properties and, as a result, suggest improved synthetic recipes as next trial conditions.

Certainly, recent reports regarding autonomous NP synthesis have demonstrated accelerated experiments aided by robotic data collections[25–36] and AI optimization modeling.[37,38] Although the significantly enhanced search efficiency is regarded as the utmost value of an autonomous laboratory, we believe that a novel chemical knowledge discovery could naturally be created since the AI robotic systems are destined to explore not only the broad range of chemical spaces but also the relationship between the reaction conditions and the corresponding material properties. In typical laboratory environments (e.g., without robotics and AI), researchers often intuitively exclude the majority of the available chemical input spaces to intentionally avoid negative results and expedite experimentation, which severely hinders new chemistry discovery. On the other hand, since no prior knowledge is provided, the AI robotic platforms in autonomous laboratories are capable of conducting broader exploration toward identifying both positive and negative results, which should be well-suited for novel chemistry discovery by revealing the effects and interdependency of certain parameters of synthetic ingredients. Despite these possible benefits, previous reports focused mainly on improving material developmental efficiency but lacked efforts to find chemical insights from the operations of AI robotic platforms.

In the process of developing new materials, a primary goal is often to discover materials that exhibit the most superior properties. For instance, when developing catalysts, the aim is to discover materials that maximize catalytic activity, selectivity, and stability. In addition, in certain cases, one may need to develop a material that satisfies multiple specified properties simultaneously. For example, researchers may seek metallic NPs with sizes of 5 nm and spherical shapes, or they may desire plate-like NPs with sizes of 10 nm. Moreover, there are situations where materials with known properties are needed but the synthesis condition remains undisclosed. Such scenarios call for a bespoke approach to tailor materials according to specific user requirements. To accelerate materials discovery, computer simulations such as density functional theory have become prevalent.[39] While these methods efficiently identify materials with the maximized properties based on the structure-property relationship, achieving bespoke design with the current computer simulation techniques remains quite challenging. In contrast, an autonomous laboratory offers a more comprehensive approach to materials development. By utilizing an autonomous laboratory, it can be feasible to determine the synthesis conditions for materials possessing desired properties on the basis of the relationship between the synthesis parameters and the material properties (i.e., a process-property relationship).

Herein, we report an autonomous laboratory for the bespoke metal NP developments with target optical properties. The platform operates based on robotic executions of the metal NP synthesis module in an aqueous medium at room temperature (RT), and UV–vis spectroscopy module as well as AI-driven exploration of synthetic recipes. Using Ag NPs as representative materials, we demonstrate that our Bayesian optimizer with the early stopping criterion successfully generates Ag NPs with target absorption spectra within only 200 iterations when optimizing across five synthetic reagents without any prior knowledge. Quantitative estimations revealed that the number of required experiments increases approximately in a linear manner with the increasing number of synthesis variables, in contrast to the grid-based search scheme in an exponential manner. In addition to the search optimization efficiency, our analysis of synthetic variables further unraveled a novel theory regarding the quantitative effects of citrate in Ag NP synthesis: The amount of citrate is key to controlling the competition between spherical and plate-shaped Ag NPs, which affects the peak intensity and peak sharpness in the absorption spectra. This work highlights that AI robotic platforms can significantly enhance material developmental efficiency and unveil previously unknown chemistry based on datasets collected using autonomous experimentations.

2. Results and Discussion

2.1. Closed-Loop NP Design in the Autonomous Laboratory

Our closed-loop operations for the NP development are schematized in **Figure 1a**. Our autonomous laboratory was designed to output Ag NPs possessing a given target absorption spectrum based on the robotic automation of metal NP batch synthesis, UV–vis spectroscopic characterization, and AI modeling. The system functions as follows: 1) the target property is given as an input: for example, Ag NPs with a maximum-intensity-wavelength (λ_{max}) of 573 nm, 2) robotic platforms operate to obtain synthesis and characterization datasets, 3) the AI model learns those datasets to suggest a better synthetic recipe or conditions, and finally, steps 2) and 3) iterate until the target property is achieved.

2.2. Hardware Setting and Automation

Figure 1b shows the bird's eye view of our hardware, where each NP synthesis module (left part of Figure 1b) and UV–vis spectroscopy module (right part of Figure 1b) are separately

C. Kim
AI-Robot Department
University of Science and Technology (UST)
Seoul 02792, Republic of Korea

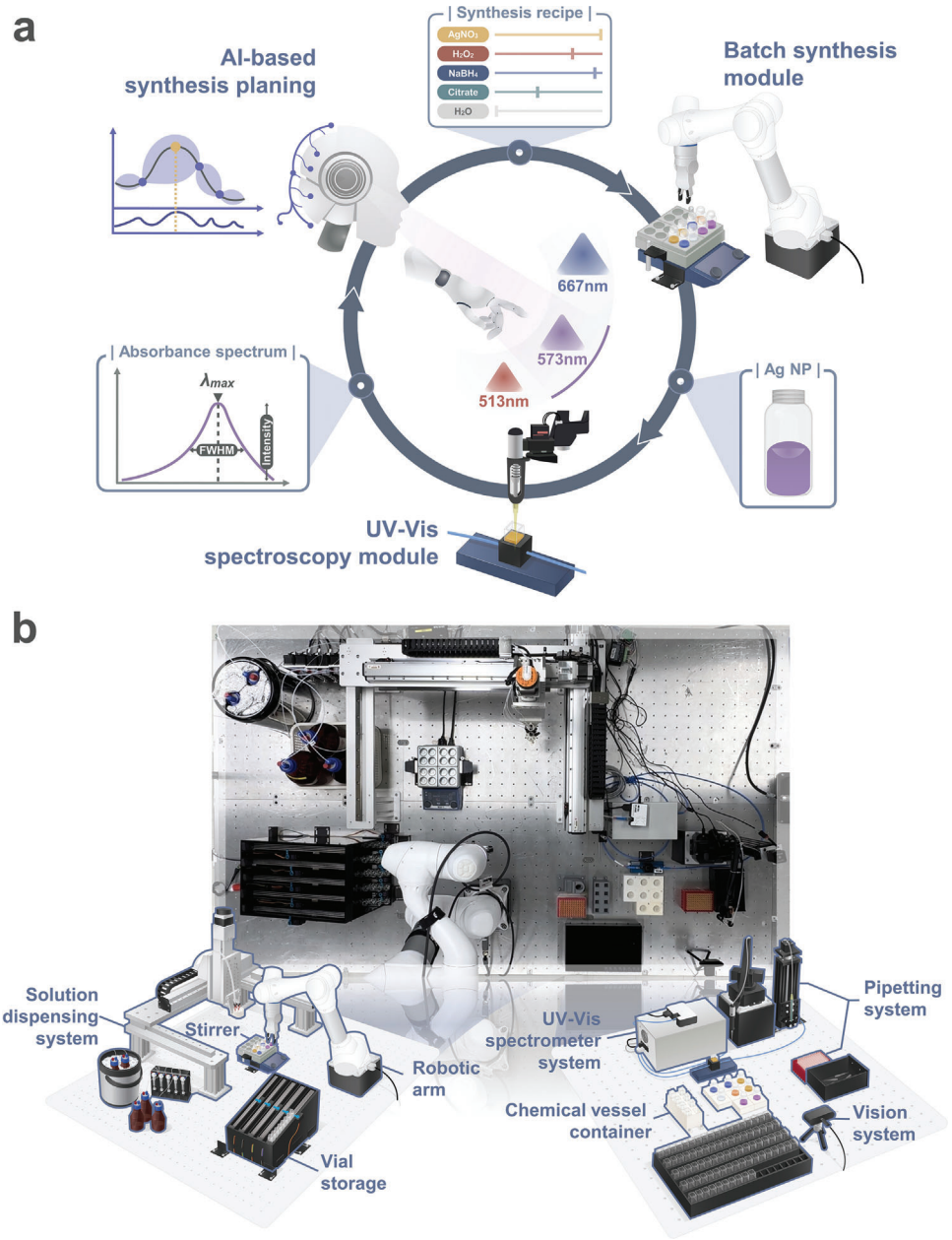

Figure 1. The autonomous laboratory platform for bespoke NP design with target optical properties. a) Scheme of the closed-loop operations for the development of Ag NPs with desired absorption spectra, as exemplified by λ_{max} of 513, 573, and 667 nm. b) A bird's eye view image of our autonomous laboratory and schematic illustrations of the batch NP synthesis module (left) and UV–vis spectroscopy module (right). The synthesis module automatically synthesizes colloidal Ag NPs, while the UV–vis spectroscopy module extracts the optical properties of the synthesized NPs. AI models optimize the synthetic recipe, although not illustrated in this figure.

shown. A video depicting hardware operations is available in Video S1 (Supporting Information) for an easier understanding of our system components and their interactions. The batch synthesis module is composed of vial storage, a stirring machine, and a solution dispensing system. The vial storage system is a self-designed two-story vial holder system where unused (empty) and used (solution-filled) vials are spatially separated in the bottom and top floors, respectively. Both floors have some gradients along the *z*-axis and are equipped with a servo motor with Arduino Uno so that the vials continuously and smoothly move down by gravity. The detailed design principles of our vial storage system are provided in Figure S2a (Supporting Information). We believe that our vial storage would be useful when applied to other types of chemical vessels, and high capacity (including 80 vials) enables closed-loop experimentations with minimized human interventions. The stirring machine supports 16 vial holders which enables the simultaneous execution of multiple synthetic experiments. The solution dispensing system

consists of a stock solution, syringe pump, dispenser, and XYZ linear actuator, as shown in Figure 1b and Figure S2 (Supporting Information). Each stock solution was stored in an ice bath to prevent the degradation of chemicals. Each syringe pump and the XYZ linear actuator precisely control the volume/rate and target positions, respectively, for the task of solution movements from the stock into vials on the stirring machine. Moreover, the UV–vis spectroscopy module (right part of Figure 1b) is composed of a chemical vessel container, pipetting system, and UV–vis spectrometer system. Note that a cuvette is a transparent and very small scale (2 mL) vessel that is prototypically used for optical measurements, and thus the pipetting system is necessary to sample the colloidal NP solutions into cuvettes based on OpenLH.[40] The movements of chemical vessels between the synthesis and characterization modules are controlled by the robotic arm with an OnRobot gripper. More detailed information about our hardware settings is provided in Figures S1–S3 (Supporting Information). Importantly, note that the batch reactor system is chosen rather than the microfluidic reactor system in our study, although the microfluidic reactor system has the advantages of lower chemical consumption and higher data generation throughput. In a larger picture, the developed NP developmental platform will be a part of the catalysis and battery design platform where both solid-state synthesis and solution-type synthesis are required. A batch reactor system with a robotic arm is a more flexible option, especially for powder-type synthesis, and therefore batch reactors are preferably adopted in our study.

It is worth noting the vision system of our autonomous laboratory (although not the main focus of this study), which is designed to detect any machine failure cases based on object detection techniques. Our systems operate without human intervention, which may lead to dangerous situations, such as imperfect vial movement and positioning. To address these safety problems and to improve the fidelity of our system, vision systems were introduced to continuously monitor operational errors at several sites including stirring machines (for vial positioning detection), cuvette holders (for cuvette positioning detection), and pipetting system (for pipette tipping detection). Our object detection model implemented in the laboratory (named DenseSSD[41]) was previously reported and was demonstrated to be much more efficient than traditional computer vision models for detecting transparent objects such as chemical vessels. At least a few hundred real scenes were collected at each monitoring site for the machine-learning training and validation of the DenseSSD model. When the model detects failure cases, it is programmed such that the whole operation is immediately halted to prevent any possible dangers. Despite the recent increasing attention to autonomous developmental systems in the materials science community, we importantly note that there is a lack of effort to address safety issues in fully robotic (researcher-free) environments. We propose that our vision-based safety alert system can become an essential component for the democratization of the autonomous material synthesis laboratory without human surveillance. More detailed information about the vision system is provided in Figure S3c (Supporting Information) as well as our previous work.[41]

Measuring instrumental errors is critical to understanding the reliability of the hardware systems. The precisions of the hardware components in both the NP synthesis and characterization modules were tested as follows. First, for the solution dispensing systems, the injection volume was precisely controlled as evidenced by the 0.999 R^2 value, which substantially outperforms conventional pipettes as shown in Figure S4a,b (Supporting Information). Second, a precision test of the pipetting system in UV–vis spectroscopic characterizations were performed in Figure S4c (Supporting Information), and a precision test of UV–vis spectrometer was performed, where the deviation in the wavelength peak position was measured to be very small at approximately only 4.35 nm, as shown in Figure S4d (Supporting Information). Using these reliable instruments, we performed the NP synthesis and UV–vis spectroscopic characterizations 100 times with identical recipes, and the deviations of three optical properties including λ_{max}, full width at half maximum (FWHM), and peak intensity were measured to be very small as shown in Figure S4e (Supporting Information), indicating that our experimental systems are highly reliable.

2.3. Synthesis Recipe Optimization Modeling

Our autonomous laboratory platform sought to synthesize Ag NPs with target optical properties that are tailored to predefined requirements. Ag NPs with specific optical properties are well known to be functional in diverse applications such as biomedical applications,[42] sensors,[43,44] light emission diodes,[45] and sensitizers of solar cells.[1–4] In particular, when mixed Ag NPs, consisting of red (absorption spectrum with λ_{max} = 513 nm), purple (λ_{max} = 573 nm), and blue (λ_{max} = 667 nm) NPs, have been used as light-trapping materials for broad light-harvesting in organic solar cells and achieved remarkable enhancement in efficiency.[3] However, since all of the three Ag NPs are commercialized, their synthesis recipes are unknown. Herein, we aim to reproduce commercialized Ag NPs via our autonomous laboratory in which the target absorption spectra are obtained from the literature.[3] We used five aqueous reagents, $AgNO_3$, H_2O_2, $NaBH_4$, citrate, and H_2O, as ingredients for Ag NP synthesis, and their volumes were parameterized in the optimization process. More details of the absorption spectra and synthesis process are shown in Figures S5 and S6 (Supporting Information). In addition, we introduced a fitness function, ranging between −1 and zero, based on the matches of three features of λ_{max}, FWHM, and peak intensity to measure the similarity of the produced property and the targeted one. The mathematical equation for the fitness function is provided in the Experimental Section and Figure S7 (Supporting Information). Out of three factors that construct the fitness function, the heaviest weights (90%) were given to the match of λ_{max} while much smaller weights (<10%) were assigned to the other two factors. We note that in general applications, these weight assignments would depend on the relevant experimental targets.

Bayesian optimization is a probabilistic optimization technique used for optimizing complex, noisy, and expensive objective functions. It is particularly valuable when the evaluation of the objective function is resource-intensive or time-consuming experiments or simulations. Owing to these benefits, Bayesian optimization has recently been considered the most effective algorithm today in realizing autonomous experimentation platforms.[27–29,33,34,36–38] We implemented Bayesian optimization with a Gaussian process regression, which interpolates

each data point as expected improvement and entropy search. Among them, the upper confidence bound (UCB) was adjusted to balance exploitation and exploration processes. Let a UCB acquisition function be defined as the following equation:

$$UCB = \mu(X) + \kappa\sigma(X), (\kappa = 10) \quad (1)$$

where $X = \{x_1,..., x_n\}$ is the vector of variables, $\mu(X)$ is the mean function, $\sigma(X)$ is the deviation and κ is the weight of exploration. To generate initial data points, Latin Hypercube Sampling[46] (LHS) was implemented to explore the data distribution evenly for each parameter, and devoid of conventional sampling artifacts (grid or random samplings). It can reflect the variation in synthesis conditions with a small amount of data. Therefore, we utilized LHS to generate 20 samples for initial data points, instead of grid or random sampling. We used the Matern kernel function, constant scaling, and noise, which can allow interpolation smoothness and experimental errors. The code of Bayesian optimization was based on past research.[36] UCB was assembled using mean, deviation, and κ. κ value was chosen as 10 in our study after a series of benchmarking tests between 2 and 20, as shown in Figure S8 (Supporting Information). It was found that, for κ value of 10, we found that exploration and exploitation were the most balanced, and the optimizer successfully reached to global optimum with great efficiency.

To maximize the search efficiency without much sacrificing the accuracy, we implemented a stopping rule named the early stopping criterion, which was conceived from the early stopping regularization method[47,48] to prevent overfitting issues in machine learning. Therefore, the early stopping function was modified to add a filter exploration process. The value of patience was set to 5, and the filter value was set to −0.1 as a hyperparameter. In our early stopping scheme, when the best fitness value (between −0.1 and zero) is not updated even after five consecutive iterations (i.e., the patience of 5), then the optimization search stops. Details of our Bayesian optimization with early stopping code implementation can be found in Figure S9 (Supporting Information) and the Data availability statement.

We used a Bayesian optimization model with the UCB function, and **Figure 2a** shows the evolution of the fitness using the Bayesian optimizer for the example of the 573 nm (λ_{max}) target property. Since the acquisition function of the UCB was applied,[28,36] exploitation and exploration were simultaneously considered, and as a result, some fluctuations in fitness were observed in Figure 2a, rather than a monotonic increase in the fitness values. Figure 2b,c shows the evolutions of the absorption spectra and five aqueous reagent volumes, respectively, as the experimental iterations proceed. For this exemplary case of the 573 nm (λ_{max}) target property, it took less than 200 iterations for the AI model to reach the optimal result. Until ≈100 iterations, the produced absorption spectra are found to be much different from the target in terms of both λ_{max} and FWHM. When the fitness first became larger than −0.1 at ≈120 iterations, we observed that λ_{max} was well matched at 573 nm after the volume control of $AgNO_3$, H_2O_2, and $NaBH_4$, but the match of FWHM was still not satisfactory. Then, further optimizations led to improved fitness at ≈175 iterations where both λ_{max} and FWHM were fit excellently after citrate volume control from 4000 to 100 µL. This tendency is generally observed that the AI model first optimizes λ_{max} with the controls of $AgNO_3$, H_2O_2, and $NaBH_4$ reagents and then later tunes FWHM with citrate controls.

Similar results for the other two cases of 513 and 667 nm target wavelengths are provided in Figures S10 and S11 (Supporting Information). For these cases, it also took less than 200 iterations for optimization, which is a surprisingly small number given that the theoretical count for a grid-based exploration for five parameters of reagent volumes is at least on the order of 10^9 in Table S3 (Supporting Information). The comparison of efficiency between autonomous search and grid-based search will be further discussed in the last result section. Due to the dominant weight of λ_{max} in the fitness function, the early iterations fit $\lambda_{max,}$ and the latter iterations more closely fit other factors of FWHM mainly based on the control of citrate volumes.

The weights in the fitness function are hyperparameters and can be set by the users' needs. In this work, the heaviest weight of 90% was given to the match of λ_{max} and the remaining 10% was assigned to the other two factors of FWHM and intensity. However, to support the general utility of our AI systems, it is worth performing additional experiments with different weight controls in the fitness function. Table S2 (Supporting Information) summarizes the weight controls of those additional experiments, and Tables S1 and S2, Figures S12 and S13 (Supporting Information) show the optimization results. For all cases, the optimizations were successfully done within 200 iterations at most, which is similar to the result of the original weight-setting case. Not surprisingly, when the highest weight was assigned to other factors of either FWHM or intensity, the strong trend of rapidly optimizing the specific factor was clearly observed in each case. We conclude that the optimizations will be well done for cases of different weight assignments; however, the optimization results will change depending on which factors users consider critically to be matched.

2.4. Analysis of Absorption Spectrum and NP Morphology

The absorption spectra obtained by our Bayesian optimizer with the early stopping criterion are presented in **Figure 3a** and are compared to the targeted spectra obtained from the literature for three cases of 513, 573, and 667 nm. These target wavelengths are only a few examples and any target absorption spectra can arbitrarily be set by users' need. Overall, they match excellently in terms of the main peak position, although some differences were observed at the shoulder peak in the lower wavelength range of 300–450 nm. These differences are attributed to the fitness function design, where the match of the main peak position (λ_{max}) and width (FWHM) are the most important parameters while the matching of other subpeaks is not considered.

Figure 3b,c highlights the morphologies of Ag NPs for each target λ_{max} case based on transmission electron microscopy (TEM) results. The average size of Ag NPs increases from 18.7 to 32.9 nm for absorption spectra with λ_{max} of 513 nm to λ_{max} of 667 nm, respectively, and this correlating trend between λ_{max} and NP size is consistent with previous reports.[1,49,50] The double peaks (main and shoulder peaks) in the absorption spectra indicate the existence of two different morphologies of NPs, i.e., spherical shapes and plate shapes. It is well known that the dif-

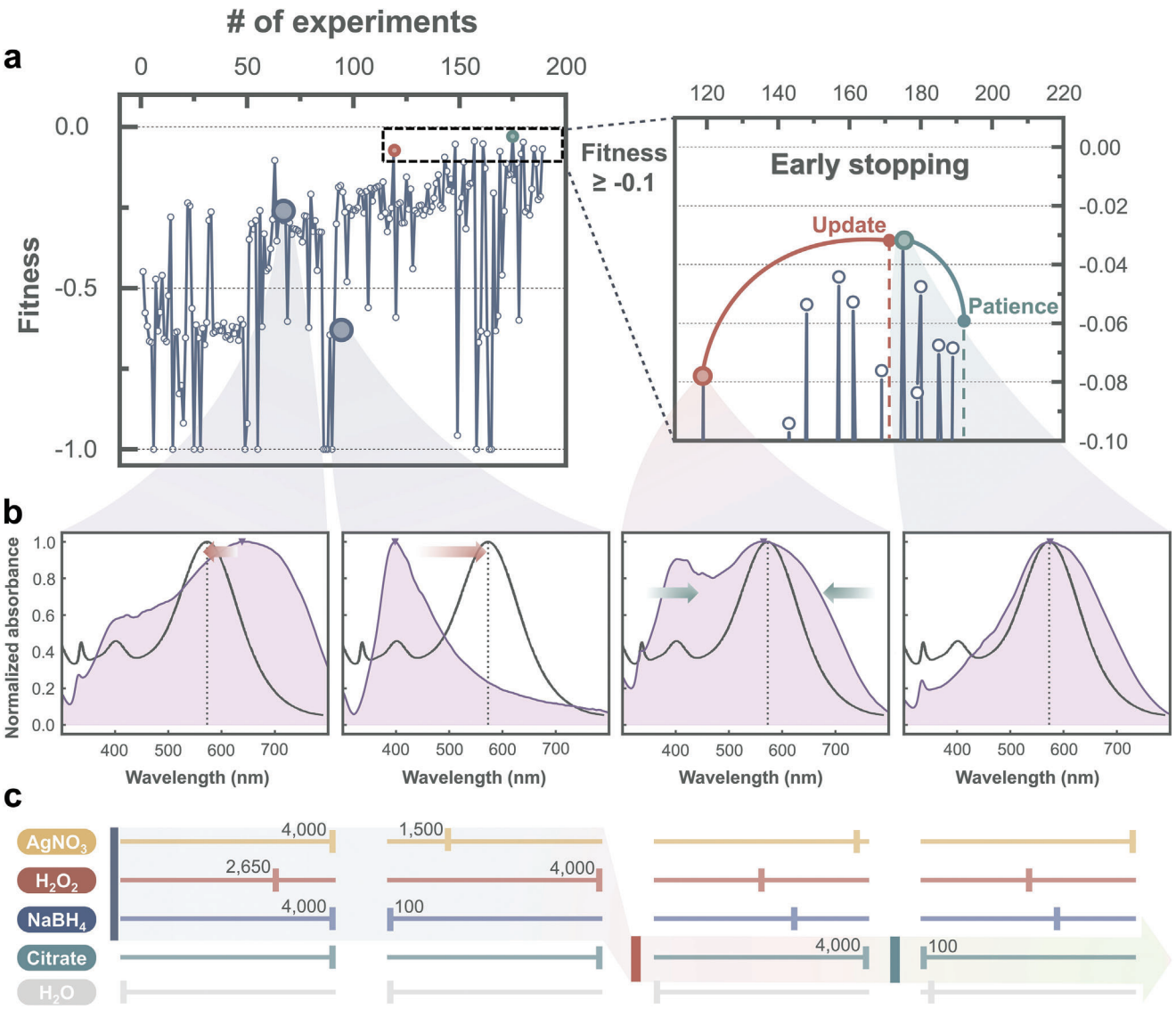

Figure 2. Bayesian optimizer with the early stopping criterion. a) The evolution of fitness values as the number of experiments progressed for the exemplary case of the 573 nm (λ_{max}) target property. The region of fitness values between −0.1 and zero is magnified on the right side. b) Evolution of the absorption spectra at various experimental iterations. The produced absorption spectra (purple area) are compared to the target spectrum (gray line) obtained from the literature in ref. [3] c) The evolution of reagent volumes at various experimental iterations (same as Figure 1b). The volume ranges were between 100 and 4000 µL for all five reagents. The arrow in shadow follows and highlights the main changes during the optimization processes and indicates that, in the early stages, the control of $AgNO_3$, H_2O_2, and $NaBH_4$ is mainly observed while the control of citrate is noticeably observed in the later phase.

ferent shapes of Ag NPs cause absorptions at different wavelengths: spherical shapes lead to absorptions at 300–450 nm[51–53] while plate shapes should be responsible for absorptions in the larger wavelength range of 450–700 nm due to the in-plane (lateral direction of the plate) dipolar resonance,[50,54,55] as agreed with the deconvolution results of UV–vis absorption spectra in Figure S14 (Supporting Information). The mixing of two different shapes (spheres and plates) was confirmed by the TEM results in Figure 3c where both triangular nanoplates and spherical NPs were observed at different ratios. We note that for the case of 513 nm, both shapes were comparably found, whereas nanoplates were dominantly found for the other two cases of 573 and 667 nm. This finding well supports that the FWHM, which is closely related to the NP size uniformity, was found to be large at 214.2 nm for the 513 nm target wavelength case, and relatively much smaller (<200 nm) for the other two cases[53–55] because the convolution of two peaks could result in a single broader peak.

It is well-known that Ag NPs exhibit the face-centered cubic (FCC) crystal structure with {111} flat facet and side facet.[56–58] TEM image analysis was performed to clarify our synthesized Ag NP facet using Titan and Technai F20 G20. In Figure S15 (Supporting Information), selected area diffraction (SAED) patterns revealed a 1/3{422} pattern with a lattice spacing of

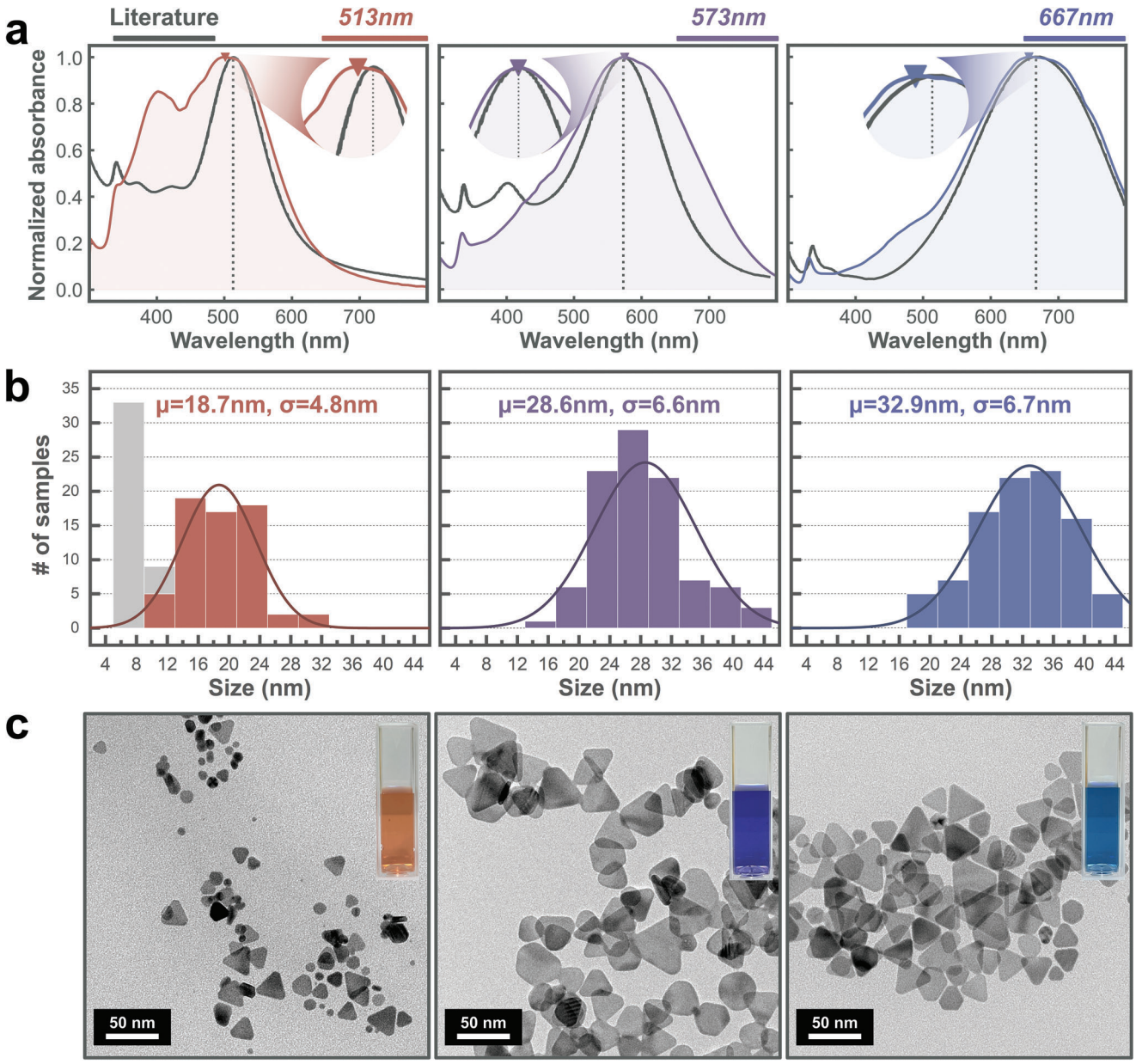

Figure 3. Analysis of UV–vis absorption spectra and NP morphologies obtained by TEM. a) Comparison of the produced absorption spectra and target spectra obtained from the literature[3] for three cases of λ_{max} values of 513, 573, and 667 nm. Spectra with the gray line represents target spectra in the literature.[3] b) The NP size distributions for the three cases based on TEM analysis. The average and deviation of NP size (μ, σ) are included. The gray box plot of 513nm describes only the Ag sphere. The line represents the Gaussian distribution of Ag nanoplate. c) Representative TEM images for the three cases. The inset images show the real scenario of colloidal NP solutions, which are diluted in cuvettes for UV–vis spectroscopic characterizations.

2.5 Å, which aligns with the [111] direction.[56–58] Additionally, {220} pattern with a lattice spacing of 1.4 Å was observed. Typically, 1/3{422} planes are not shown in Ag FCC crystals, and these observations suggest the existence of multiple {111} twin planes parallel to the basal plane, which indicates a specific crystallographic structure of Ag nanoplate.[56–58] Furthermore, the side facets oriented in the [110] direction exhibited {111} reflections with a lattice spacing of 2.36 Å. More detailed the preparation of TEM samples is explained in Experimental Section.

2.5. SHAP-Based Interpretation of Synthesis Variables

Using the datasets accumulated from the autonomous experiments, we performed SHapley Additive exPlanations (SHAP)[59] analysis to measure the influence of synthesis variables of five input reagents, and the results for each target wavelength (λ_{max}) are presented in **Figure 4**. Independent of the target wavelengths, the volumes of $AgNO_3$ and H_2O_2 are strongly influential parameters whereas those of citrate and H_2O are weakly influential. The significant effects of $AgNO_3$ (metal source), H_2O_2 (oxidant),

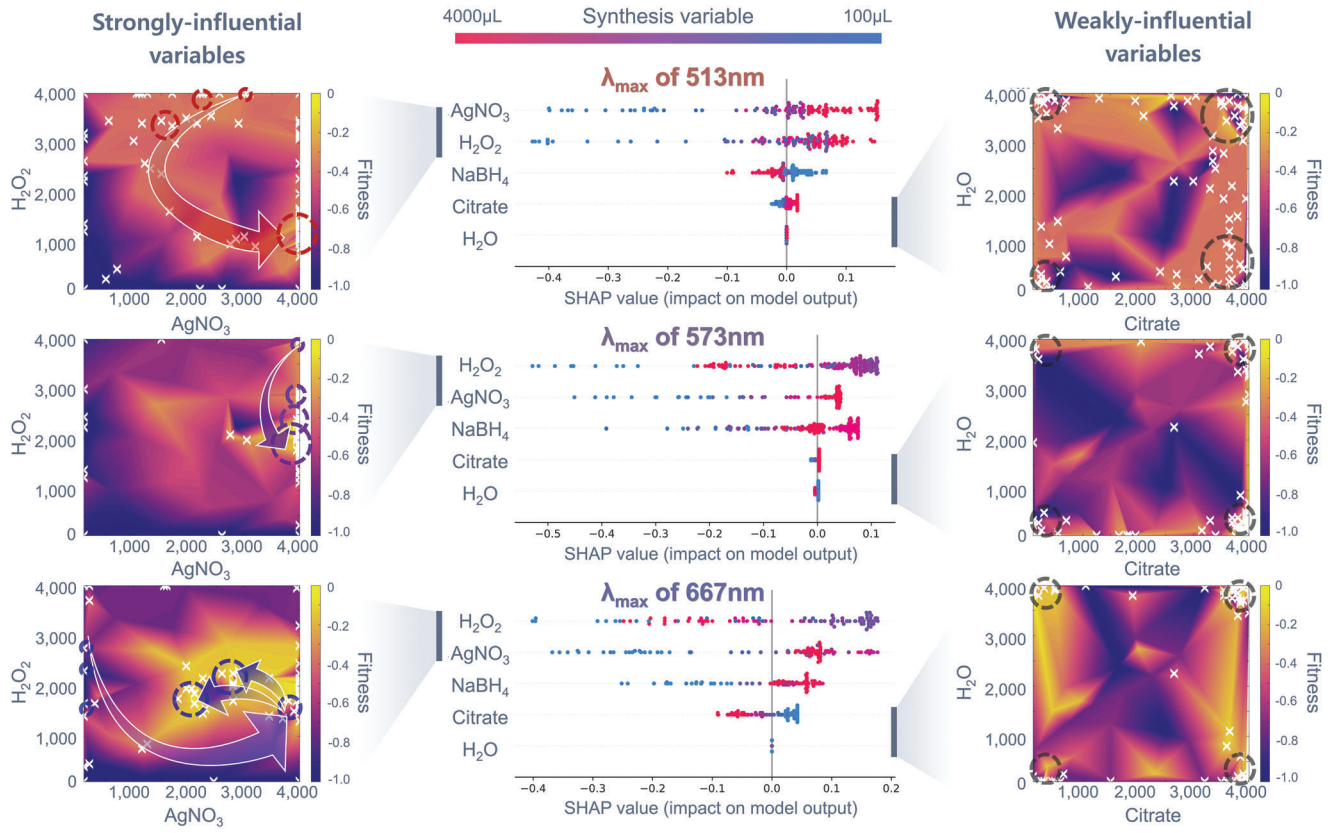

Figure 4. SHAP-based interpretation of synthetic variables. The SHAP analyses are shown in the center, for three cases of λ_{max} values of 513, 573, and 667 nm. In each case, the reagent with the highest impact is positioned on the top, while those with the lower impact follow. The color represents the volume of each synthetic reagent between 100 and 4000 μL. Each left and right column show the evolutions of two strongly influential variables and two weakly influential variables in the fitness map, respectively. The circles and arrows in the fitness maps highlight the synthetic routes during optimizations.

and $NaBH_4$ (reductant) reagents on NP morphologies and properties are well documented in many previous reports,[51,54,60–62] and agree well with our SHAP analysis.

Based on the SHAP analysis, the trajectories of synthesis variables during optimizations are investigated, as shown in Figure 4 where the strongly influential variables ($AgNO_3$, H_2O_2) and the weakly influential variables (citrate, H_2O) are separately visualized in two-dimensional fitness maps. The data clearly show that AI broadly explores the full volume range for $AgNO_3$ and H_2O_2, and that, on the contrary, the explorations are relatively limited for citrate and H_2O. These conclusions are confirmed by dense search points only in the corners of the corresponding fitness maps of Figure 4. Such different observations likely occur because the volume changes of citrate or H_2O have relatively little effect on λ_{max}, and thus there are weaker driving forces for the AI model to explore the full volume range of these reagents broadly. This result can explain the restricted impact of citrate on FWHM and H_2O on intensity, with their contributions assigned a low weight in the fitness function. For all target wavelength cases, it was consistently found that the fitness becomes terrible when the H_2O_2 volume is too large likely because NPs are too oxidized and, as a result, decompose into Ag ions (Ag^+).[43,62] It was also found that the volume ratio of H_2O_2 to $AgNO_3$ ($H_2O_2/AgNO_3$) is strongly correlated with λ_{max} as shown in Figure S16 (Supporting Information) and other literature[60–62] and thus would serve as a crucial descriptor for controlling peak positions in the absorption spectra.

2.6. Discovery of Novel Chemical Knowledge from Autonomous Experimentations

Although the SHAP analysis in Figure 4 revealed that, out of five synthetic ingredients, the volume of citrate is the least influential parameter on λ_{max} of the absorption spectra, its effects on FWHM and absorption peak intensity were found clearly noticeable as shown in Figure 2b,c. In **Figure 5**a where the absorption spectrum results of two extreme citrate volumes (100 and 4000 μL) were compared with all other conditions being identical, the lower volume of citrate causes stronger and sharper absorption peaks, i.e., higher peak intensity and smaller FWHM in Figure 5a. This trend is attributed to different NP morphologies confirmed from TEM images where NPs tend to be spherical for the 100 μL case and were mainly formed as plate shapes for 4000 μL. Importantly, we note that the quantitative effects of citrate concentrations have not been clearly manifested thus far in the literature,[51,54,60–62] and the comparative results allowed us to identify that the amount of citrate is key to controlling the competition between spherical and plate-shaped Ag NPs and resultant UV–vis absorption spectra.

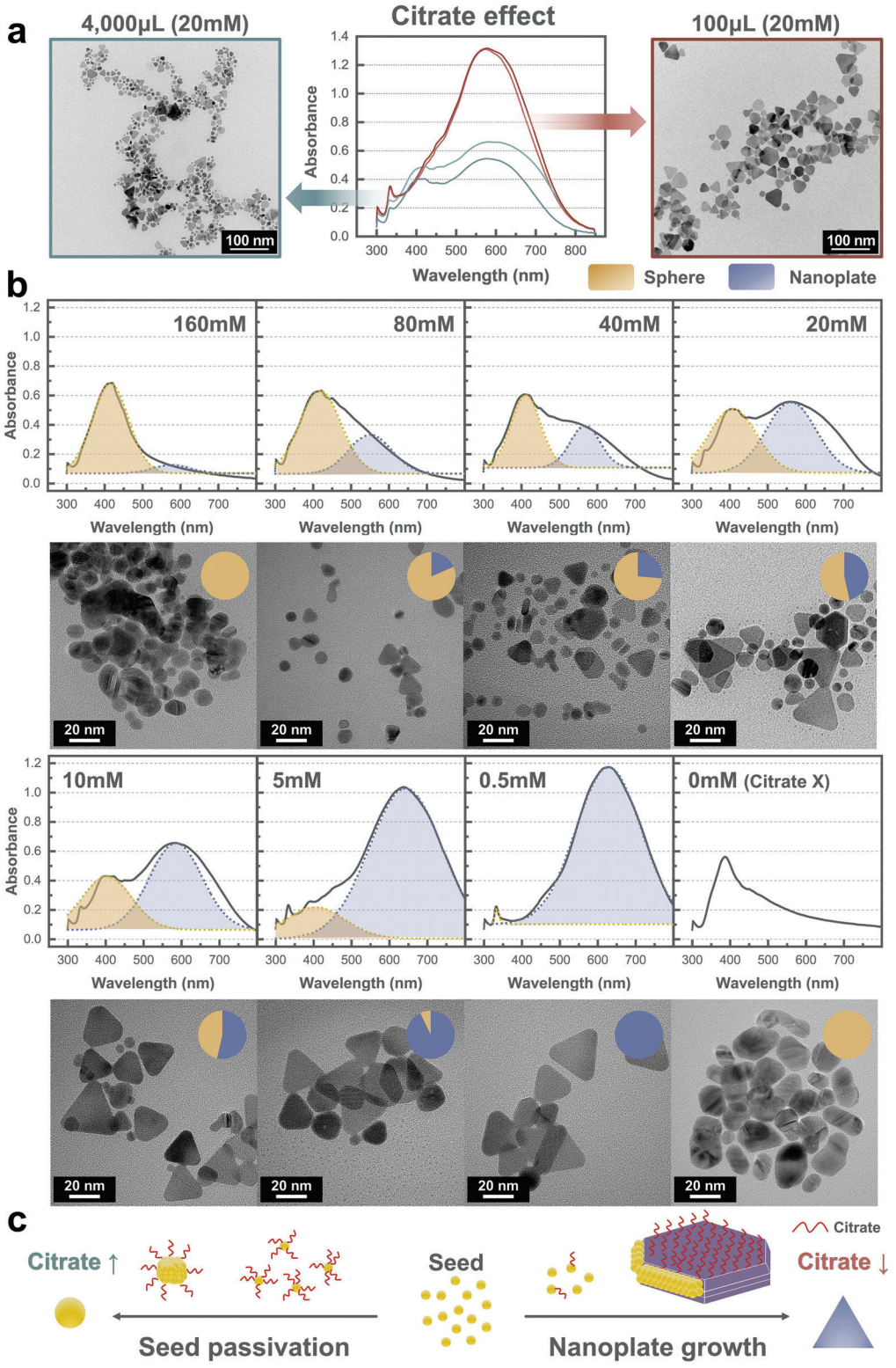

Figure 5. The quantitative effect of citrate on Ag NP synthesis and UV–vis absorption spectra. a) Comparisons of absorption spectra and NP morphologies (TEM images) between citrate volumes of 100 μL (red lines) and 4000 μL (green lines). b) The changes in absorption spectra and the corresponding NP morphologies (TEM images) with variations in citrate concentrations from 0 mM (no use) to 0.5 mM (diluted) to 160 mM (extremely concentrated). The absorption spectra are deconvoluted with two peaks contributed by spherical NPs and plate-shaped NPs. The inset pie chart in the TEM images represents the ratio between two NP shapes, with blue denoting plate shapes and yellow denoting spherical shapes. c) Schematic of citrate effects on Ag NP growth kinetics and mechanisms.

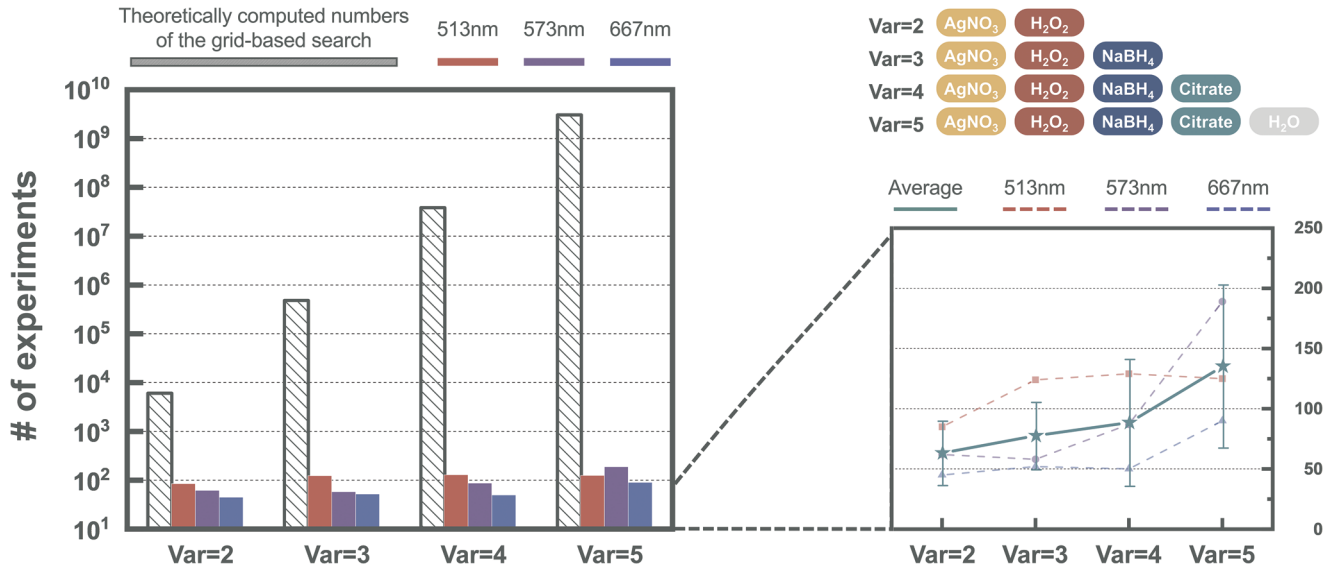

Figure 6. Quantitative estimations of AI-based optimization efficiency. The number of experiments to complete the optimizations was shown with varying synthesis variables. The number of synthesis variables is progressively controlled from two to five, based on the SHAP impact order in Figure 4. To better understand the optimization efficiency, the results were compared to the theoretically computed numbers of the grid-based search scheme. The AI modeling results are magnified on the right side.

To systematically explore the quantitative effects of citrate in a broader range, we parameterized the citrate concentrations from 0 to 160 mM in Figure 5b instead of controlling the citrate volume since the volume control range is limited up to the vessel capacity. From the deconvolution analyses of the absorption spectra, we found that a peak around the wavelength of 400 nm dominates over the other peak at ≈600 nm for higher concentration cases. The peak at ≈400 nm is contributed by the spherical NPs while that ≈600 nm is attributed to the nanoplates, and these two peaks formed with different ratios depending on the citrate concentrations, as shown in Figure 5b and Figure S17 (Supporting Information). For the 160 mM case, spherical NPs were almost exclusively found while nanoplates were dominantly found for the other extreme case of 0.5 mM. Note that NPs were not produced without citrate (0 mM case), which was also well reported in previous studies.[51,54] This analysis adequately explains the experimental observation that the FWHM is the largest at ≈300 nm at intermediate concentration levels (10–20 mM) due to the convolution of comparably strong peaks. A more detailed analysis of citrate concentration controls and their quantitative effects is shown in Figure S18 (Supporting Information).

The quantitative effects of citrate concentrations on NP shapes can be readily understood from the growth kinetics, as schematized in Figure 5c. Citrate tends to preferably adsorb on Ag {111} surfaces due to the stronger binding energy,[63–66] which results in anisotropic NP growth, i.e., plate shapes. However, if sufficient amounts of citrates were given during the NP synthesis, they adsorb on all available binding sites on both {111} and other surfaces such as [110] directional surfaces, which likely leads to isotropic NP growth, i.e., spherical shapes. We emphasize that, unlike many other recent studies of autonomous material synthesis[25–36] which mainly focused on enhancing the search efficiency based on the combined approach of robotics and AI modeling, our study highlights the two capabilities for improved search efficiency and uncovering a novel chemical knowledge (in this case, the quantitative effect of citrate on NP formation) by analyzing the datasets collected autonomous experiments.

The knowledge we acquired from this study mainly includes both the optimized synthetic routes and the novel chemical knowledge regarding the quantitative effects of citrate in Ag NP synthesis. We believe that the role of each reagent will also be valid in the large-scale batch synthesis as well (NP synthesis of kilogram or tons unit);[67] however, the final results could be inevitably affected by some external factors that were not considered in smaller lab-scale setting, such as mass and heat transfer[68,69] behaviors in larger reaction vessels. In other words, these macro-kinetic factors should also be treated as critical parameters, which would quantitatively influence the optimized synthetic routes or the chemical knowledge.

2.7. Quantitative Estimations of Search Efficiency

To quantitatively understand the search efficiency of our Bayesian optimizer, we measured the number of experiments required to complete the optimization with an increasing number of synthetic reagents, as shown in **Figure 6**. These synthesis variables were progressively added from two to five in the order of their previously determined SHAP impact (Figure 4), i.e., $AgNO_3$ → H_2O_2 → $NaBH_4$ → citrate → H_2O. The efficiency of the AI model was estimated by comparing it to theoretically computed numbers of the grid-based search scheme which is also known as a full factorial design. Here, the grid-based search indicates that, if each parameter range is divided into N grids for M synthetic reagents, then the exploration number over the whole chemical space would scale exponentially as N^M. Note that N is set as 78 in our study given that the large volume control ranges between 100 and 4000 μL, as shown in Figure S19 (Supporting

Information). As the number of synthesis variables linearly increases, grid-based explorations would become exponentially expensive, which severely limits the practical uses of such grid-based schemes. On the other hand, our AI-based search is significantly more efficient, completing the optimizations within 200 iterations for all three cases of different target wavelengths (513, 573, and 667 nm), as shown in Figure 6 and Table S3 (Supporting Information). We emphasize that this search efficiency depends on the number of variables. Unlike the grid-based search, the number of required experiments increases approximately in a linear manner with the increasing number of synthesis variables, and this feature should be highly beneficial when exploring complex chemical spaces involving multiple parameters.

Since the search efficiency is likely affected by the initial sampling, we tried various seed numbers in Latin Hypercube Sampling (LHS) to generate various sets of initial data points and see how the search efficiency would be affected by the choice of initial sampling. The test results are summarized in Figure S20 (Supporting Information) where 20 initial data points were generated for each seed number of LHS. For five different sets of initial samplings, we demonstrated that the number of required experiments to reach the optimum point was all similar ≈100 iterations (between 86 and 117), which supports that our AI optimization model provides excellent repeatability in terms of AI optimization process and search efficiency.

We also note particular features of some traditional approaches in the Design of Experiments (DOE), including LHS and the Taguchi method.[70] LHS is basically a type of random sampling approach that uniformly distributes the sampling points over the whole parameter space. Although LHS ensures wide explorations, its search efficiency is similar to that of grid-based search. The Taguchi method[70] is also one of the widely employed approaches in DOE. This method nicely reflects the variations of parameters but is limited when exploring interdependent synthesis variables,[71] which is a common case in most material synthesis experiments (for example, the interdependency between the reagent volume parameter and concentration parameter). Unlike traditional DOE approaches, AI modeling, such as Bayesian optimizations, exhibits evident benefits, including a balanced search mechanism between exploitation and exploration, and significantly enhanced optimization efficiency particularly in high-dimensional parameter spaces.

3. Conclusion

Although the demonstrations presented in this work were performed on synthesizing Ag NPs and characterizing optical properties, our presented platforms and closed-loop experimental workflows can be readily expanded to other materials such as multicomponent NPs and other properties that may be desired in respective applications such as catalysis, solar cells, and sensors. The study of autonomous material development is only in its infancy, and thus, several limitations need to be resolved shortly to enable broad applicability.

First, from a hardware point of view, some experimental tools and protocols need to be designed to be more robot-friendly rather than human-in-the-loop. In the autonomous laboratory, human interventions will be only minimal, and robotic executions will be dominant. However, most of the experimental hardware equipment that is commercially available today requires manual intervention, which sometimes makes the robotic operations extremely challenging to execute simple human-enabled tasks.[72] For example, rotating the cap of vials (a type of chemical vessel) is an easy task for humans, but requires difficult and time-consuming processes for robots. Second, from a software point of view, the AI models need to be substantially advanced. Efforts to find the global minimum with the best search efficiency, even in a complex chemical space, need to be continued. In the future, the next-generation AI models should solve for categorical variables (synthesis sequences, selections/sequences of operations and chemicals, etc.), in addition to continuous variables (such as solution volumes, concentrations, and injection rate).

In summary, we developed and reported an autonomous laboratory platform for the bespoke design of Ag NPs with target optical properties. This platform operates in a closed-loop manner between the batch synthesis module and UV–vis spectroscopy module, in which the experimental planning and decision-making were performed by a Bayesian optimizer implemented with the early stopping criterion. Our work emphasizes the value of autonomous experimentation platforms, which offer twofold benefits of enhancing material developmental efficiency and elucidating novel chemical knowledge by analyzing the datasets accumulated from the operations of AI robotic platforms.

4. Experimental Section

Chemical Reagents: Silver nitrate ($AgNO_3$), sodium citrate dihydrate (citrate), 30 wt% hydrogen peroxide solution (H_2O_2), and sodium borohydride ($NaBH_4$) were purchased from Sigma–Aldrich. All reagents were used as received. All stock solutions were based on distilled water. As shown in Figure S2c (Supporting Information), solutions of $NaBH_4$ and H_2O_2 were stored in the ice bucket and changed every 12 h to delay the potential degradation of the reductant and oxidant. For NP precipitations, 99.8% acetone was purchased from Daejung Reagent.

Batch Synthesis: $AgNO_3$ solution (1.25 mM), citrate solution (20 mM), H_2O_2 solution (0.375 wt%), $NaBH_4$ (10 mM), and DI water were stored in brown bottles to protect them from light illumination. The chemical reactants were chosen from the literature.[51,54] The reason for controlling the discrete variable is that the solution dispensing system has an error of ≈1–2 µL, so it is given discretely as 50 µL to make the AI model robust if several dispensing errors occur in the hardware. To prepare nanoparticle synthesis, a robotic arm picks vials up and puts them inside a constrained location of a stirrer for a uniform synthesis process, as can be seen in Figure S2b-2 (Supporting Information). In the synthesis process sequence, $NaBH_4$, DI water, citrate, and H_2O_2 were sequentially injected with a solution dispensing system and stirred for five minutes to mix evenly on a stirrer. After that, $AgNO_3$ was added and stirred for 40 min at 800 rpm at RT. The vials were not sealed in the work due to possible explosion risk when hydrogen gas is involved in the NP reduction process. Instead, to minimize solvent vaporization, the whole synthesis process was performed at RT, and all stock solutions were based on DI water. The nanoparticle synthesis was performed for 40 min, and vials containing synthesized nanoparticles were moved to the UV–vis spectroscopy module. All processes of the batch synthesis module are shown in Video S1 (Supporting Information).

Optical Spectroscopic Characterizations: After NP synthesis is completed, the robotic arm places the solution-filled vials into a vial holder. Then, the arm locates the cuvette from storage to the holder and places the cuvette into the UV–vis spectroscopic testing holder to obtain optical properties. The absorption spectra data were extracted by a spectrometer through an optical fiber, and a light source was used to obtain reference and absorbance data. The cuvette was filled to 2 mL with DI water, and

the colloidal nanoparticle solution was injected to 0.8 mL and mixed three times via a robotic arm and linear actuator pump. The pipetting system was followed by OpenLH.[40] The Scipy library, including the *find_peaks*, *peak_prominences*, and *peak_widths* functions, was used for the extraction of optical properties. All processes of the UV–vis spectroscopy module are also shown in Video S1 (Supporting Information).

Fitness Function: Fitness is an evaluation function to measure the degree of match between two absorption spectra. This can be computed as follows:

$$\text{Fitness function} = -0.9 \times \frac{\left|\lambda_{\max} - \lambda_{\max,\ target}\right|}{A_{\lambda_{\max}}} - 0.07 \times (1 - intensity) - 0.03 \times \frac{FWHM}{A_{\text{FWHM}}} \quad (2)$$

The fitness function reflects λ_{max}, FWHM, and peak intensity for the absorption spectra of nanoparticles. This implies multi-objective optimization for the bespoke synthesis of NPs, although the highest weight was assigned to the λ_{max} term because the λ_{max} property has the highest priority for organic solar cell applications.[3] These weight assignments would depend on the researchers and the relevant experimental targets. The range of absorption spectra was considered from 300 to 850 nm depending on the UV–vis spectrometer. The main purpose of introducing denominators such as $A_{\lambda_{max}}$ or A_{FWHM} is normalization (placing between 0 and 1) so that each factor (excluding pre-weights) can be treated fairly. The wavelength range that was considered in this study was between 300 and 850 nm. In order to keep $\frac{|\lambda_{max} - \lambda_{max,\ target}|}{A_{\lambda_{max}}}$ between 0 and 1 for normalization purposes, $A_{\lambda_{max}}$ was chosen as the distance from the target wavelength to the farthest boundary wavelength (either 300 or 850 nm). As shown in Figure S7b (Supporting Information), for the example of $\lambda_{max} = 513$ nm, $A_{\lambda_{max}}$ was computed as 337 nm (850 nm−513 nm). For the other example of $\lambda_{max} = 667$ nm, $A_{\lambda_{max}}$ was computed as 367 nm (667 nm−300 nm). A_{FWHM} is constantly set as 550 nm (= |300−850|), which is the full wavelength range of consideration in this study. Although the total volume of the reactions was not kept constant in each measurement and these variations may slightly affect the absorbance intensity, the effect of solution volumes on fitness values was found very limited, even less than 0.02. More detailed information on the fitness function is described in Figure S7 (Supporting Information).

TEM Analysis: After NP synthesis was completed, 0.5 mL of the sample was placed into the 1 mL microcentrifuge tube. For precipitation of the NP, 0.5 mL of acetone was added before sonication for 5 min. Then, it was centrifuged at 13 500 rpm for 20 min. After the surfactant was removed, 0.1 mL of DI water was added. The carbon gird (200 Mesh, Copper) was placed to filter paper on the petri dish. The prepared sample (5 µL) was drop cast three or four times. TEM equipment (FEI Technai F20 G20, FEI Titan) was used to obtain the morphology data of the Ag NPs and selected area diffraction (SAED) patterns of Ag NPs. ImageJ was used to measure the size distribution in TEM images.[73]

SHAP Analysis: SHapely Addictive exPlanations[59] (SHAP) analysis is a game theoretic approach to calculate the influence order of variables when the model predicts some outputs. A higher SHAP value implies a large impact of the variable on the model. *KernelExplainer* with *LogitLink* utilizes weighted linear regression to compute SHAP values from models for each epoch cumulatively through experimental data. The SHAP values were implemented to draw the bee swarm plot colored by the value of the synthesis variable via the *summary_plot* function. The fitness surface based on the accumulated experimental data points was also visualized, as shown in Figure 4. Here, each experimental datum is composed of a synthesis recipe and fitness value. The fitness surface was made based on the linear interpolation libraries implemented in MATLAB.

Supporting Information

Supporting Information is available from the Wiley Online Library or from the author.

Acknowledgements

This work was supported by the National Research Foundation of Korea funded by the Ministry of Science and ICT (NRF-2022M3H4A7046278) and the IITP grant (No. 2021-0-02076) funded by the Korean government (MSIT).

Conflict of Interest

The authors declare no conflict of interest.

Author Contributions

H.J.Y. and N.K. contributed equally to this work. S.S.H., D.K., and K.-Y.L. conceived the idea and supervised the project. H.J.Y. and N.K. performed hardware settings for the automation of NP synthesis and characterizations. H.J.Y. developed Bayesian optimizer with the early stopping criterion and fitness function. N.K. implemented an XAI approach to enable interpretable data insights. H.J.Y., N.K., H.L., and D.K. performed experiments for data collection. H.J.Y., N.K., H.L, D.K., H.N., C.K., and S.Y.L. verified experimental data and TEM analysis. L.C.O.T. and H.J.Y. developed vision systems based on object detection models. All authors contributed to the results discussion and manuscript writing.

Data Availability Statement

Several result data are provided in the following GitHub repository (https://github.com/KIST-CSRC/BespokeSynthesisPlatform/tree/main/Result). Each datum consists of a synthesis recipe, raw spectra data, and optical properties. The codes and relevant explanations that are required for the autonomous laboratory functioning are available in the GitHub repository. They are provided in the following three github addresses: the platform (https://github.com/KIST-CSRC/BespokeSynthesisPlatform), batch synthesis module (https://github.com/KIST-CSRC/BatchSynthesisModule), and UV-vis spectroscopy module (https://github.com/KIST-CSRC/UV–visModule). All codes are written over Python 3.7 and all environments can be created through the requirements.txt file.

Keywords

autonomous laboratory, Bayesian optimization, bespoke material design, chemical knowledge discovery, metal nanoparticle synthesis

Received: October 11, 2023
Revised: February 15, 2024
Published online:

[1] T. Putnin, C. Lertvachirapaiboon, R. Ishikawa, K. Shinbo, K. Kato, S. Ekgasit, K. Ounnunkad, A. Baba, *Opto-Electronic Adv.* **2019**, *2*, 19001001.
[2] A. R. Mallah, M. N. M. Zubir, O. A. Alawi, S. N. Kazi, W. Ahmed, R. Sadri, A. Kasaeian, *Renew. Energy.* **2022**, *187*, 1204.
[3] A. Phengdaam, S. Nootchanat, R. Ishikawa, C. Lertvachirapaiboon, K. Shinbo, K. Kato, S. Ekgasit, A. Baba, *J. Sci. Adv. Mater. Devices.* **2021**, *6*, 264.
[4] D. H. Wang, J. K. Kim, G.-H. Lim, K. H. Park, O. O. Park, B. Lim, J. H. Park, *RSC Adv.* **2012**, *2*, 7268.
[5] B. Hvolbæk, T. V. W. Janssens, B. S. Clausen, H. Falsig, C. H. Christensen, J. K. Nørskov, *Nano Today* **2017**, *2*, 14.

[6] T. Reier, M. Oezaslan, P. Strasser, *ACS Catal.* **2012**, *2*, 1765.
[7] H. W. Lee, H. Nam, G.-H. Han, Y.-H. Cho, B. C. Yeo, M.-C. Kim, D. Kim, K.-Y. Lee, S. Y. Lee, S. S. Han, *Acta Mater.* **2021**, *205*, 116563.
[8] P. D. Howes, R. Chandrawati, M. M. Stevens, *Science* **2014**, *346*, 1247390.
[9] Y. Khaniani, Y. Ma, M. Ghadiri, J. Zeng, D. Wishart, S. Babiuk, C. Charlton, J. N. Kanji, J. Chen, *Sci. Rep.* **2022**, *12*, 12850.
[10] C. J. Neal, A. Gupta, S. Barkam, S. Saraf, S. Das, H. J. Cho, S. Seal, *Sci. Rep.* **2017**, *7*, 1324.
[11] Y. Xia, Y. Xiong, B. Lim, S. E. Skrabalak, *Angew. Chemie. Int. Ed.* **2009**, *48*, 60.
[12] R. Emil, *Chem. Soc. Rev.* **2006**, *35*, 583.
[13] E. Galati, M. Tebbe, A. Querejeta-Fernández, H. L. Xin, O. Gang, E. B. Zhulina, E. Kumacheva, *ACS Nano* **2017**, *11*, 4995.
[14] M. Abolhasani, A. Oskooei, A. Klinkova, E. Kumacheva, A. Günther, *Lab on a Chip* **2014**, *14*, 2309.
[15] Z. Xu, H. Gao, H. Guoxin, *Carbon* **2011**, *49*, 4731.
[16] D.-Y. Kim, R. G. Saratale, S. Shinde, A. Syed, F. Ameen, G. Ghodake, *J. Clean. Prod.* **2018**, *172*, 2910.
[17] D. Chen, X. Qiao, X. Qiu, J. Chen, *J. Mater. Sci.* **2009**, *44*, 1076.
[18] S. Agnihotri, S. Mukherji, S. Mukherji, *RSC Adv.* **2014**, *4*, 3974.
[19] N. G. Bastús, F. Merkoçi, J. Piella, V. Puntes, *Chem. Mater.* **2014**, *26*, 2836.
[20] C. H. Kwak, S.-M. Kang, E. Jung, Y. Haldorai, Y.-K. Han, W.-S. Kim, T. Yu, Y. S. Huh, *J. Ind. Eng. Chem.* **2018**, *63*, 405.
[21] D. Kim, S. Jeong, J. Moon, *Nanotechnology* **2006**, *17*, 4019.
[22] I. Ojea-Jiménez, N. G. Bastús, V. Puntes, *J. Phys. Chem. C.* **2011**, *115*, 15752.
[23] E. Izak-Nau, A. Huk, B. Reidy, H. Uggerud, M. Vadset, S. Eiden, M. Voetz, M. Himly, A. Duschl, M. Dusinska, I. Lynch, *RSC Adv.* **2015**, *5*, 84172.
[24] W. Jin, G. Liang, Y. Zhong, Y. Yuan, Z. Jian, Z. Wu, W. Zhang, *Nanoscale Res. Lett.* **2019**, *14*, 81.
[25] C. W. Coley, D. A. Thomas, J. A. M. Lummiss, J. N. Jaworski, C. P. Breen, V. Schultz, T. Hart, J. S. Fishman, L. Rogers, H. Gao, R. W. Hicklin, P. P. Plehiers, J. Byington, J. S. Piotti, W. H. Green, A. J Hart, T. F. Jamison, K. F. Jensen, *Science* **2019**, *365*, eaax1566.
[26] S. Steiner, J. Wolf, S. Glatzel, A. Andreou, J. M. Granda, G. Keenan, T. Hinkley, G. Aragon-Camarasa, P. J. Kitson, D. Angelone, L. Cronin, *Science* **2019**, *363*, eaav2211.
[27] S. Langner, F. Häse, J. D. Perea, T. Stubhan, J. Hauch, L. M. Roch, T. Heumueller, A. Aspuru-Guzik, C. J. Brabec, *Adv. Mater.* **2020**, *32*, 1907801.
[28] R. W. Epps, M. S. Bowen, A. A. Volk, K. Abdel-Latif, S. Han, K. G. Reyes, A. Amassian, M. Abolhasani, *Adv. Mater.* **2020**, *32*, 2001626.
[29] K. Higgins, S. M. Valleti, M. Ziatdinov, S. V. Kalinin, M. Ahmadi, *ACS Energy Lett.* **2020**, *5*, 3426.
[30] A. A. Volk, R. W. Epps, D. T. Yonemoto, B. S. Masters, F. N. Castellano, K. G. Reyes, M. Abolhasani, *Nat. Commun.* **2023**, *14*, 1403.
[31] H. Zhao, W. Chen, H. Huang, Z. Sun, Z. Chen, L. Wu, X. F. Yu, *Nat. Synth.* **2023**, *2*, 505.
[32] D. Salley, G. Keenan, J. Grizou, A. Sharma, S. Martín, L. Cronin, *Nat. Commun.* **2020**, *11*, 2771.
[33] H. Tao, T. Wu, S. Kheiri, M. Aldeghi, A. Aspuru-Guzik, E. Kumacheva, *Adv. Funct. Mater.* **2021**, *31*, 2106725.
[34] F. Mekki-Berrada, Z. Ren, T. Huang, W. K. Wong, F. Zheng, J. Xie, I. P. S. Tian, S. Jayavelu, Z. Mahfoud, D. Bash, K. Hippalgaonkar, S. Khan, T. Buonassisi, Q. Li, X. Wang, *npj Comput. Mater.* **2021**, *7*, 55.
[35] Y. Jiang, D. Salley, A. Sharma, G. Keenan, M. Mullin, L. Cronin, *Sci. Adv.* **2022**, *8*, eabo2626.
[36] B. Burger, P. M. Maffettone, V. V. Gusev, C. M. Aitchison, Y. Bai, X. Wang, X. Li, B. M. Alston, B. Li, R. Clowes, N. Rankin, B. Harris, R. S. Sprick, A. I. Cooper, *Nature* **2020**, *583*, 237.
[37] F. Häse, L. M. Roch, C. Kreisbeck, A. Aspuru-Guzik, *ACS Cent. Sci.* **2018**, *4*, 1134.
[38] F. Häse, M. Aldeghi, R. J. Hickman, L. M. Roch, A. Aspuru-Guzik, *Appl. Phys. Rev.* **2021**, *8*, 031406.
[39] B. C. Yeo, H. Nam, H. Nam, M. C. Kim, H. W. Lee, S. C. Kim, S. O. Won, D. H. Kim, K.-Y. Lee, S. Y Lee, S. S Han, *npj. Comput. Mater.* **2021**, *7*, 137.
[40] G. Gome, J. Waksberg, A. Grishko, I. Y. Wald, O. Zuckerman, in *TEI 2019 – Proceedings of the 13th Int. Conf. on Tangible Embedded, and Embodied Interaction*. **2019**, 55.
[41] L. C. O. Tiong, H. J. Yoo, N. Kim, C. Kim, K.-Y. Lee, D. H. Kim, S. S Han, *npj. Comput. Mater.* **2024**, *10*, 42.
[42] S. Farooq, F. Dias Nunes, R. E. de Araujo, *Photonics Nanostructures – Fundam. Appl.* **2018**, *31*, 160.
[43] M. Zannotti, V. Vicomandi, A. Rossi, M. Minicucci, S. Ferraro, L. Petetta, R. Giovannetti, *J. Mol. Liq.* **2020**, *309*, 113238.
[44] K. M. Mayer, J. H. Hafner, *Chem. Rev.* **2011**, *111*, 3828.
[45] J. Saade, C. B. De Araújo, *Mater. Chem. Phys.* **2014**, *148*, 1184.
[46] E. L. Melnick, B. S. Everitt, *Encyclopedia of Quantitative Risk Analysis and Assessment*, Wiley, Hoboken, NJ **2008**.
[47] Z. Dai, H. Yu, K. H Low, P. Jaillet, *Int. Conf. on Machine Learning*, **2019**, PMLR, 1496–1506.
[48] A. Makarova, H. Shen, V. Perrone, A. Klein, J. B. Faddoul, A. Krause, C. Archambeau, *Int. Conf. on Automated Machine Learning*. **2022**.
[49] D. Aherne, D. M. Ledwith, M. Gara, J. M. Kelly, *Adv. Funct. Mater.* **2008**, *18*, 2005.
[50] I. Pastoriza-Santos, L. M. Liz-Marzán, *J. Mater. Chem.* **2008**, *18*, 1724.
[51] Q. Zhang, N. Li, J. Goebl, Z. Lu, Y. Yin, *J. Am. Chem. Soc.* **2011**, *133*, 18931.
[52] S. Linic, P. Christopher, D. B. Ingram, *Nat. Mater.* **2011**, *10*, 911.
[53] K. L. Kelly, E. Coronado, L. L. Zhao, G. C. Schatz, *J. Phys. Chem.* **2003**, *107*, 668.
[54] M. Tsuji, S. Gomi, Y. Maeda, M. Matsunaga, S. Hikino, K. Uto, T. Tsuji, H. Kawazumi, *Langmuir* **2012**, *28*, 8845.
[55] A. Brioude, M. P. Pileni, *J. Phys. Chem. B.* **2005**, *109*, 23371.
[56] Q. Zhang, Y. Hu, S. Guo, J. Goebl, Y. Yin, *Nano letters* **2010**, *10*, 5037.
[57] A. L. Beulze, E. Duguet, S. Mornet, J. Majimel, *Langmuir* **2014**, *30*, 1424.
[58] M. Dong, R. Fu, H. Min, Q. Zahng, H. Dong, *Crystal Growth & Design* **2021**, *21*, 1314.
[59] T. Martin, *Interpretable Machine Learning*, 1st ed., Chapman & Hall /CRC, Florida **2019**.
[60] N. Li, Q. Zhang, S. Quinlivan, J. Goebl, Y. Gan, Y. Yin, *ChemPhysChem.* **2012**, *13*, 2526.
[61] T. Parnklang, C. Lertvachirapaiboon, P. Pienpinijtham, K. Wongravee, C. Thammacharoen, S. Ekgasit, *RSC Adv.* **2013**, *3*, 12886.
[62] K. Wongravee, T. Parnklang, P. Pienpinijtham, C. Lertvachirapaiboon, Y. Ozaki, C. Thammacharoen, S. Ekgasit, *Phys. Chem. Chem. Phys.* **2013**, *15*, 4183.
[63] H. Xu, B. J. Wiley, *Chem. Mater.* **2021**, *33*, 8301.
[64] X. C. Jiang, C. Y. Chen, W. M. Chen, A. B. Yu, *Langmuir* **2010**, *26*, 4400.
[65] J. Zeng, J. Tao, W. Li, J. Grant, P. Wang, Y. Zhu, Y. Xia, *Chem. – An Asian J.* **2011**, *6*, 376.
[66] D. S. Kilin, O. V. Prezhdo, Y. Xia, *Chem. Phys. Lett.* **2008**, *458*, 113.
[67] A. Flegler, S. Wintzheimer, M. Schneider, C. Gellermann, K. Mandel, *Handbook of Nanomaterials for Industrial Applications*, Elsevier, **2018**, 137–150.
[68] R. Paliwal, R. J. Babu, S. Palakurthi, *AAPS Pharm. Sci. Tech* **2014**, *15*, 1527.
[69] A. V. Nikam, B. L. V. Prasad, A. A. Kulkarni, *CrystEngComm* **2018**, *20*, 5091.
[70] S. Maghsoodloo, G. Ozdemir, V. Jordan, C. H. Huang, *Journal of Manufacturing* **2004**, *23*, 73.

[71] H. Tao, T. Wu, M. Aldeghi, T. C. Wu, A. Aspuru-Guzik, E. Kumacheva, *Nat. Rev. Mater.* **2021**, *6*, 701.
[72] Y. Jiang, H. Fakhruldeen, G. Pizzuto, L. Longley, A. He, T. Dai, A. I. Cooper, *Digital Discovery* **2023**, *2*, 1733.
[73] C. Rueden, C. Dietz, M. Horn, J. Schindelin, B. Northan, M. Berthold, K. Eliceiri, ImageJ Ops [Software] https://imagej.net/Ops (accessed: November 2021).